Robust SAR Image Registration Using Rank-Based Ratio Self-similarity

Xin Xiong, Guowang Jin, Qing Xu, and Hongmin Zhang

***Abstract*—Synthetic aperture radar (SAR) images in different polarizations or from different sensors are becoming easily available, but registering these images is challenging because of the presence of significant speckles in SAR images and the existence of radiometric differences between images. To address the problems, we propose a novel feature descriptor named rank-based ratio self-similarity (RRSS) for robust SAR image registration. The descriptor first calculates a ratio surface by replacing the distance surface, as the use of the ratio is more robust to multiplicative noise, and then sorts the ratio values to construct the rank surface. Subsequently, the rank surface is partitioned into an index map, and the index map is then transformed into the descriptor vector based on a restricted adaptive binning grid to discriminatively describe features. Furthermore, a rotation invariance enhancement method is designed for the RRSS descriptor to efficiently calculate descriptor vectors in multiple orientations. We conduct experiments with six SAR image pairs of various bands, polarizations, and resolutions from different sensors, including ALOS-PALSAR, Gaofen-3, Sentinel-1, and TerraSAR-X. The results demonstrate that the proposed descriptor is superior to state-of-the-art descriptors and robust for SAR image registration.**

***Index Terms*—Image registration, rank, ratio self-similarity, synthetic aperture radar (SAR) image.**

I. Introduction

SYNTHETIC aperture radar (SAR) images are an indispensable remote sensing data type because they are available at all times and under all weather conditions [1]. Hence, they are useful for diverse applications, such as image fusion, change detection, and 3-D reconstruction. Image registration is a basic process for these applications, the goal of which is to align two or more images of the same scene captured by the same or different sensors from different viewpoints or at different times [2]. Due to the existence of geometric as well as radiometric differences between the images and the presence of significant multiplicative speckles in the SAR images, SAR image registration is still a challenging task.

Image registration has made great progress in recent decades. Generally, the existing image registration methods can be divided into two categories: intensity-based methods and feature-based methods [3]. The intensity-based methods compare predefined templates to search for optimal correspondences using different kinds of similarity metrics, such as mutual information (MI) [4], normalized cross-correlation coefficient (NCC) [5], and cross-cumulative residual entropy [6]. Recently, some works based on cross-correlation have been published in SAR image registration [7], [8]. Although methods of this type can achieve high accuracy, they are sensitive to geometric differences and need substantial computational time for searching optimal correspondences [9], [10].

Feature-based methods are more robust to geometric differences and are generally faster than intensity-based methods [11]. These methods extract salient image features (i.e., points, lines, and regions) and identify reliable feature correspondences by matching feature descriptors. In recent decades, numerous feature-based methods were developed. Among them, scale-invariant feature transform (SIFT) [12] is the most representative because of its invariance to scale, rotation, and brightness. Numerous SIFT-like methods have been proposed for SAR image registration to reduce the influence of speckles. Methods of this type include SIFT-OCT [13], which skips the features detected at the first octave of the scale space pyramid; the bilateral filter SIFT (BFSIFT) [14], adapted anisotropic Gaussian SIFT (AAG-SIFT) [15], and nonlinear diffusion scale space SIFT (NDSS-SIFT) [16], which use a bilateral filter, adapted anisotropic Gaussian filter, and nonlinear diffusion method, respectively, instead of a Gaussian filter to construct scale spaces; and SAR-SIFT [17], which defines a new gradient obtained from the ratio of the exponentially weighted averages (ROEWA) algorithm. Another related and interesting method is the one followed in [18], which combines image segmentation and SIFT. Although the abovementioned methods have been successfully applied to SAR image registration, they still face two problems. The first is a lack of controllability in the number and distribution of extracted features. Several studies have been devoted to solving this problem by using feature selection strategies [19]–[21]. Another problem, which has not been effectively solved, is that the process of orientation assignment tends to be unreliable for SAR images due to the interference of speckles [22], [23].

Additionally, radiometric differences exist between SAR images acquired in different polarizations or by different SAR

Manuscript received October 28, 2020; revised December 13, 2020 and January 9, 2021; accepted January 22, 2021. Date of publication January 28, 2021; date of current version February 15, 2021. This work was supported in part by the National Natural Science Foundation of China under Grant 41071296, Grant 41474010, and Grant 61401509, and in part by the Outstanding Youth Foundation of Information Engineering University under Grant 2016603502. *(Corresponding author: Xin Xiong.)*

Xin Xiong, Guowang Jin, and Qing Xu are with the Institute of Geospatial Information, PLA Strategic Support Force Information Engineering University, Zhengzhou 450001, China (e-mail: xiongxinhbhh@163.com; guowang_jin@163.com; 13937169139@139.com).

Hongmin Zhang is with the Institute of Data and Target Engineering, PLA Strategic Support Force Information Engineering University, Zhengzhou 450001, China (e-mail: zhmin1206@163.com).

Digital Object Identifier 10.1109/JSTARS.2021.3055023

sensors. Therefore, it is challenging to register such images. Recently, Shechtman and Irani [24] introduced a descriptor named LSS, which captures the shape properties of images. LSS is stable to complex radiometric differences and has been successfully applied to multispectral remote sensing image registration [25]. Because of their insensitivity to radiometric differences, several LSS-based descriptors have been developed. Sedaghat *et al.* [26], [27] proposed the distinctive order-based self-similarity (DOBSS) descriptor and the histogram of oriented self-similarity (HOSS) descriptor for multisensor optical image matching. Ye *et al.* [28] introduced a descriptor named the dense LSS (DLSS) by integrating LSS descriptors of multiple small regions for optical-to-SAR image template matching. Our previous work [29] designed a novel descriptor named the rank-based local self-similarity (RLSS), which used rank values instead of correlation values. The RLSS descriptor was also integrated to form the dense RLSS (DRLSS) descriptor for optical-to-SAR image template matching. Although some improvements in robustness have been made in the above-mentioned LSS-based descriptors, the discriminability of these descriptors is relatively poor in reliably distinguishing features of SAR images as they are sensitive to speckles.

To solve the aforementioned limitations, an improved LSS descriptor, named rank-based ratio self-similarity (RRSS), is proposed for robust SAR image registration. In the descriptor, the distance surface is replaced by a ratio surface to suppress the speckles, and the rank surface is extracted from the ratio surface to enhance the discriminability. Then, the rank surface is partitioned into an index map, and the index map is transformed into a descriptor vector based on a restricted adaptive binning (RAB) grid. Furthermore, to avoid the process of orientation assignment, a rotation invariance enhancement method is designed for the proposed descriptor.

The main contributions of this study are as follows.

1) An RRSS descriptor is proposed by constructing the rank surface from the ratio surface to increase the distinctiveness against radiometric differences and the robustness to speckles.
2) Based on the RAB grid, a rotation invariance enhancement method is designed for the RRSS descriptor, which can efficiently calculate descriptor vectors in multiple orientations.
3) A comprehensive evaluation is made with state-of-the-art methods using various SAR image pairs.

This article extends our previous work of the RLSS descriptor [29] in two aspects. On the one hand, a Gaussian weighted ratio surface that is robust to image speckles is designed, which replaces the distance surface to construct the rank surface. On the other hand, the rotation invariance enhancement method is adopted, which is based on the RAB grid instead of the log-polar grid.

The remainder of this article is organized as follows. The proposed SAR image registration method is introduced in Section II, with an emphasis on the construction of the RRSS descriptor. Experimental results are presented in Section III. Finally, the conclusion is given in Section IV.

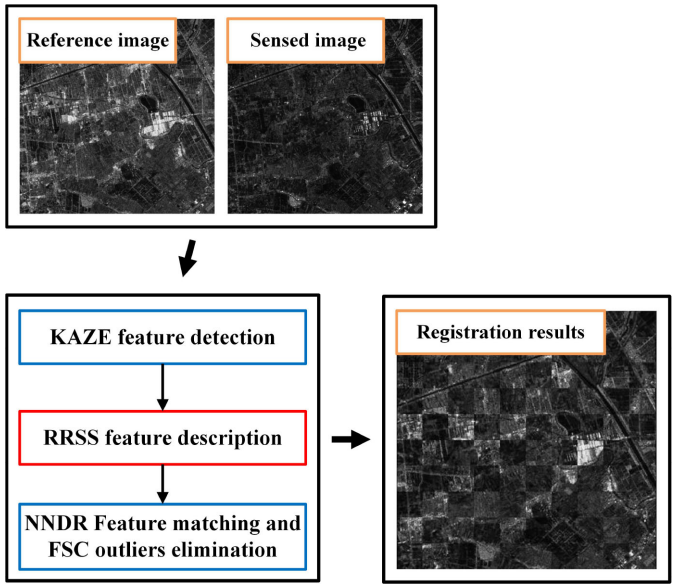

Fig. 1. Flowchart of proposed method.

II. Methodology

This section details the proposed method for robust SAR image registration. The proposed method includes three main steps, as illustrated in Fig. 1. First, a KAZE detector [30], [31] is used to extract reliable and sufficient feature points. Then, the proposed RRSS descriptor is introduced to distinctively describe these features. Finally, the nearest neighbor distance ratio (NNDR) matching strategy [12] followed by the fast sample consensus (FSC) algorithm [32] are performed to identify the effective matches. After the three main steps, the sensed image can be resampled to generate the registered image. The details of the proposed method are presented in the following sections.

A. KAZE Detector

Typical feature point detectors include corner detectors such as features from an accelerated segment test (FAST) [33], Harris [34], and SAR-Harris [17], and blob detectors such as SIFT [12], speeded-up robust features (SURF) [35], and KAZE [31]. Compared to corner detectors, blob detectors are more suitable for LSS-based descriptors. This is because these descriptors are very sensitive to the central patch of the local region (the small neighborhood of the feature point), and the small neighborhood of the blob points is more stable for pixel position errors than that of the corner points. In addition, due to its excellent boundary retention ability, nonlinear diffusion filtering was introduced into the Harris detector to extract highly repetitive feature points under strong radiometric changes [36]. As a blob detector, KAZE detects feature points in nonlinear scale spaces generated by nonlinear diffusion filtering. Therefore, the KAZE detector is used for detecting stable and sufficient feature points.

KAZE detects maximum response values of the scale-normalized determinant of the Hessian at multiple scale levels

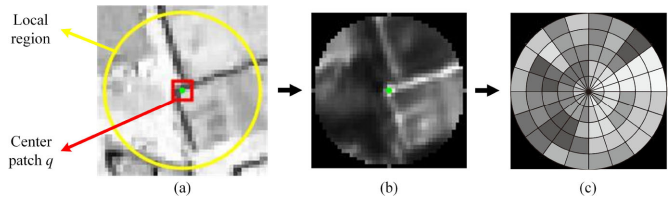

Fig. 2. LSS descriptor generation. (a) Local feature region. (b) Correlation surface. (c) Log-polar translated LSS descriptor.

as candidate feature points. That is,

$$L_{\text{Hessian}} = \sigma^2 \left(L_{xx} L_{yy} - L_{xy}^2 \right) \tag{1}$$

where L_{xx}, L_{yy}, and L_{xy} are the second-order horizontal, vertical, and cross derivatives, respectively. σ is the scale factor. More details of the KAZE detector are well studied in [31].

B. LSS Descriptor

The proposed RRSS descriptor is an improved version of the LSS descriptor. Before the RRSS descriptor is presented, the LSS descriptor is briefly reviewed. The LSS descriptor is robust to radiometric variations by capturing the shape properties of the image [24]. It extracts local self-similar features of the center patch and generates a descriptor vector based on the log-polar grid.

The process of LSS descriptor generation is shown in Fig. 2. In the local region centered at q (typically 20 pixels in radius and $S \times S$: 41×41 pixels in size), the distance surface $\text{SSD}_q(x, y)$ is obtained by calculating the sum of square differences (SSD) between the central patch (typically $P \times P$: 5×5 pixels in size) and all surrounding patches,

$$\text{SSD}_q(x, y) = \| M_q(0, 0) - M_q(x, y) \|_2^2 \tag{2}$$

where $M_q(0, 0)$ and $M_q(x, y)$ represent the matrices of the central patch and the surrounding patch, respectively. Then, $\text{SSD}_q(x, y)$ is transformed into the correlation surface $S_q(x, y)$,

$$S_q(x, y) = \exp\left(-\frac{\text{SSD}_q(x, y)}{\max\left(\text{var}_{\text{noise}}, \text{var}_{\text{auto}}(q)\right)} \right) \tag{3}$$

where $\text{var}_{\text{noise}}$ is a constant corresponding to acceptable radiometric variations, and $\text{var}_{\text{auto}}(q)$ is the maximal variance of the difference of all patches within a very small neighborhood of q (1 pixel in radius) relative to the central patch. The correlation surface $S_q(x, y)$ is then transformed into a log-polar grid and partitioned into 80 bins (20 angular bins and 4 radial bins). The maximal correlation value in each bin is selected to generate the descriptor vector. Finally, this descriptor vector is linearly normalized to enhance the radiometric invariance.

C. RRSS Descriptor

The main limitation of the LSS descriptor for SAR image registration is its relatively low discriminability. There are two reasons for this. One reason is that the correlation surface is sensitive to speckles, and thus, the descriptor cannot reliably distinguish different features. Another reason is that the values of the correlation surface for various local dissimilar features are relatively low, but these features may be valid for finding the correct correspondence. We propose the RRSS descriptor to enhance the discriminability of the LSS descriptor. The construction process of the proposed descriptor is illustrated in Fig. 3. In the following, the details of the proposed descriptor are presented.

1) Ratio Surface Construction: Different from constructing the distance surface using SSD in LSS, we construct a new distance surface $\text{RS}_q(x, y)$, called the ratio surface, by calculating the ratio between the central patch and all surrounding patches, as follows:

$$\text{RS}_q(x, y) = \min\left\{ \frac{M_q(0, 0)}{M_q(x, y)}, \frac{M_q(x, y)}{M_q(0, 0)} \right\}. \tag{4}$$

On the ratio surface, the adjacent pixel values are strongly correlated because the adjacent surrounding patches overlap. Due to the correlation effects, the ratio surface will lose information, which prevents reliable feature description. To reduce the correlation effects, we introduce a Gaussian weight function. Then, the weighted ratio surface is

$$\text{WRS}_q(x, y) = G \cdot \min\left\{ \frac{M_q(0, 0)}{M_q(x, y)}, \frac{M_q(x, y)}{M_q(0, 0)} \right\}. \tag{5}$$

The standard deviation of the Gaussian function is set to $(P - 1)/4 = 1$ based on multiple experiments.

2) Rank Surface Construction: The next step is to construct the rank surface. Inspired by Spearman's rank correlation coefficient or Spearman's Rho, the rank values can replace the intensity values for the correlation calculation [37]. The rank is the relative position label or the order in the data list after sorting (for example, descending order). It assesses monotonic relationships rather than linear relationships, and thus, it is robust to nonlinear radiometric differences between images. In LSS, the features that are not similar to the central patch are missing in the correlation surface. The rank values can be used as substitutes for correlation values to reveal part of the missing information, as shown in Fig. 4. Considering that (3) is a composite of multiple functions and some of the functions are monotonic, the calculation of the weighted ratio surface can be simplified to calculate the rank surface,

$$\text{RWRS}_q(x, y) = R\left(\text{WRS}_q(x, y)\right) \tag{6}$$

where R represents the operation of obtaining the rank values by sorting. Compared with (3), (6) increases the sorting operation but reduces the calculation of the monotonic functions. Note that the feature points on different scale layers have different sizes of circular neighborhoods ($k\sigma$ pixels in radius). The neighborhoods are resampled to uniform circular regions (20 pixels in radius) for calculating the rank surface.

Then, the rank surface is transformed into an index map by partitioning the rank values. The number of pixels in the rank surface is M, and the rank, thus, has a value range of $[1...M]$. The value range is equally divided into three bins, and the bin indices are sequentially numbered from 1 to 3. Here, the number of bins is recommended to be 3 based on multiple experiments. Therefore, each pixel of the rank surface has a unique bin index, and the index map can be obtained.

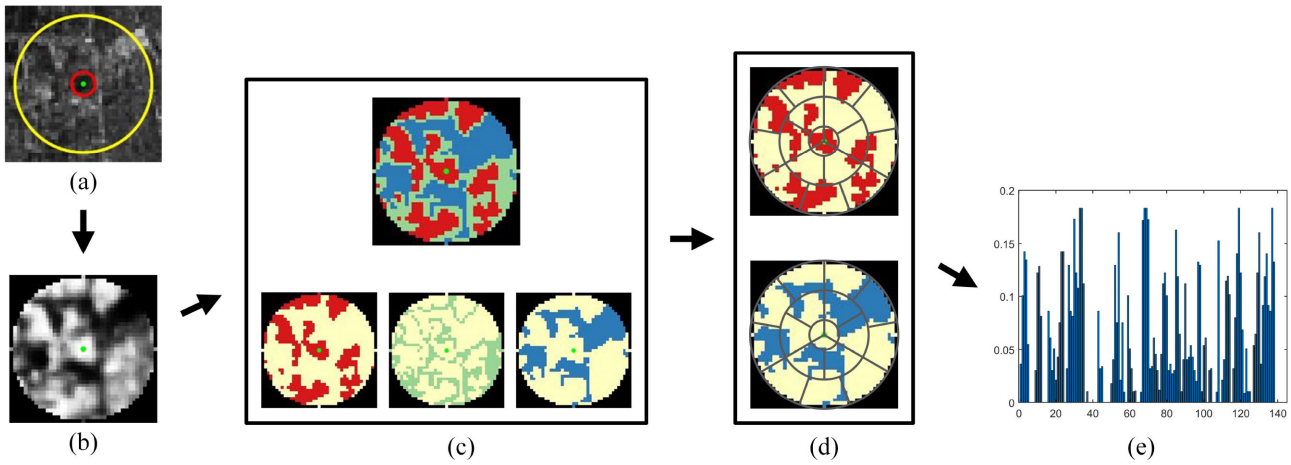

Fig. 3. Process of RRSS descriptor construction. (a) Local region. (b) Rank surface. (c) Index map. (d) Gridded index map. (e) RRSS descriptor.

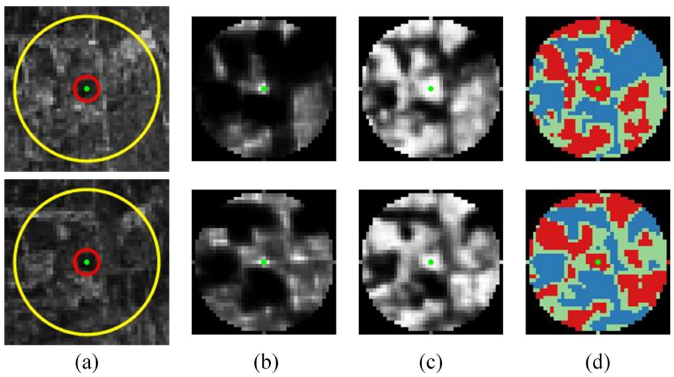

Fig. 4. (a) Normalized local regions of image pair from ALOS-PALSAR, up: HH polarization; down: HV polarization. (b) Correlation surfaces. (c) Rank surfaces. (d) Index maps. In index maps, pixels numbered 1, 2, and 3 are marked in red, green, and blue, respectively.

3) Grid Representation: The purpose of grid representation is to divide the index map into multiple grid bins. LSS that uses a regular log-polar grid is sensitive to pixel position errors since the inner circular region is too small. Among the well-known representation methods, descriptors with a log-polar grid (GLOH [38] and DAISY [39]) are more adaptive to geometric distortion than a descriptor with a square grid (SIFT) [12], but the inner circular region is not divided into radial sectors, which decreases the descriptor distinctiveness since some spatial information is lost [40].

The adaptive binning [40] grid is adopted for grid representation. By partitioning the inner circular ring into fewer angular bins than the outer circular ring in the descriptor structure, the adaptive binning grid can avoid pixel location errors and increase descriptor distinctiveness. r stands for the number of radial bins, and set $A = \{a_1, \ldots, a_r\}$ is applied as the number of angular bins. Fig. 3(d) provides an illustration of grid representation by adaptive binning for $r = 3$, $A = \{3, 6, 9\}$.

4) Descriptor Vector Generation: After grid representation of the index map, the numbers of pixels with different index values in each bin are counted, and the ratios of the counted numbers to the total number of pixels in the grid bin are taken as the descriptor values. The ratio values for indices 1 and 3 are retained, and those for index 2 are ignored. There are two reasons for this. On the one hand, the ratio values for the three indices are strongly related because their sum is 1. Thus, it is redundant to use all three ratio values as the descriptor values. On the other hand, pixels with indexes 1 or 3 are usually aggregated. Their ratio values can better capture the local shape properties than index 2. Fig. 3(c) shows an example index map and three index submaps split from it. It can be found that the pixels with index 1 or 3 are aggregated, while those with index 2 are scattered.

The descriptor values of a bin are

$$V_{i,j} = W_{i,j}/M_{i,j}, \quad i = 1, \ldots, r \quad j = 1, \ldots, a_i \tag{7}$$

where $W_{i,j} = [\, w_{i,j}^1 \; w_{i,j}^3 \,]$ is the counted number of pixels with indices 1 and 3, and $M_{i,j}$ is the total number of pixels in the bin. $V_{i,j} = [\, v_{i,j}^1 \; v_{i,j}^3 \,]$ is the descriptor value of the bin. Subscripts i and j identify the position of the bin in the grid structure.

Then, the descriptor values of all bins are connected to generate the descriptor vector D as follows:

$$D = [D_1, \ldots, D_r], \quad D_i = [V_{i,1}, \ldots, V_{i,a_i}] \tag{8}$$

where D_i is the descriptor subvector for the ith ring. Obviously, the dimension of the descriptor vector is $2\sum_{i=1}^{r} a_i$. To gain invariance to radiometric changes, the vector finally needs to be normalized.

D. Rotation Invariance of the RRSS Descriptor

The previous section analyzed the possibility of RRSS for feature description and described the details of the descriptor vector generation. Note that the construction process of the abovementioned descriptor is based on the assumption that there are no rotations between the two images; that is, rotation differences are not considered. Undeniably, in most application scenes, the rotation differences between remote sensing images are very small. In addition, the images can be directly georeferenced using navigation information so that the rotation and scale differences between images can be significantly reduced [41].

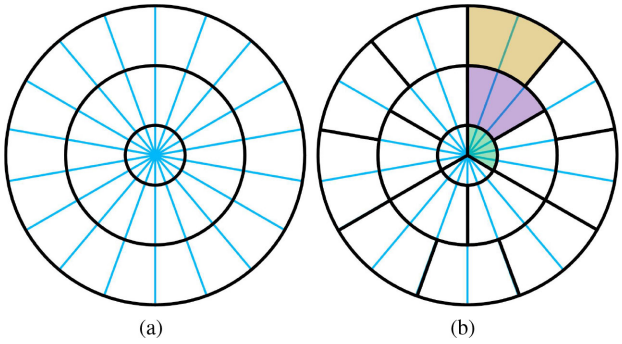

Fig. 5. Geometric relationship between (a) regular log-polar grid and (b) RAB grid.

However, the result is usually a local optimum to match an image pair with rotation differences, even if the differences are not significant. Therefore, the rotation differences cannot be ignored, and special processing must be performed to keep the descriptor rotationally invariant.

The most straightforward method is to perform the orientation assignment similar to SIFT [12]. However, the method fails primarily for two reasons. On the one hand, the angular bins need to be densely divided according to the optimal numbers of angular bins given in Section III-B, which brings about the need to accurately estimate the dominant orientation. On the other hand, the descriptor captures the aggregated shape features, and thus, the dominant orientation is difficult to estimate very accurately.

To eliminate the effect of rotation differences, a rotation invariance enhancement method is designed by building a descriptor vector for each feature point in the reference image and seven descriptor vectors with different orientations for each feature point in the sensed image. The orientation values are equally spaced and are set as $L = [-3l, -2l, -l, 0, l, 2l, 3l]$. l is the orientation spacing. Each orientation can be assigned to generate a descriptor vector. It should be noted that the process of generating multiple descriptor vectors is time-consuming. To improve the computational efficiency, an acceleration scheme is designed. In the stages of the grid representation and descriptor vector generation, the initial descriptor vector can be generated by a log-polar grid with dense radial bins, and then the initial result is compressed into descriptor vectors in multiple orientations under certain rules. The rules are derived from the geometric relationship between a regular log-polar grid and an RAB grid, as shown in Fig. 5.

1) Initial Descriptor Vector Generation: The initial descriptor vector is captured in a regular log-polar grid. The radial rings are divided into b radial bins. Set $b = 360l$ so that when multiple orientations are assigned, the values of the descriptor are not changed, and only the order of the descriptor vector is rotated, which avoids capturing descriptor values an extensive number of times in the grid. The initial descriptor values for bin (i, j) are

$$U_{i,j} = W_{i,j} W_{i,j} / M_{i,j} \quad i = 1, \ldots, r \quad j = 1, \ldots, b. \tag{9}$$

The initial descriptor vector for the ith ring is

$$R_i = [U_{i,1}, \ldots, U_{i,b}]. \tag{10}$$

2) Multiorientation Descriptor Vector Generation: The order of R_i is rotated according to the specified orientation index s, $s = [-3, -2, -1, 0, 1, 2, 3]$, to obtain descriptor vectors for the ith ring in seven orientations, as follows:

$$E_i^s = \left[T_{i,1}^s, \ldots, T_{i,b}^s\right] = \begin{cases} [U_{i,b+s+1}, \ldots, U_{i,b}, U_{i,1}, \ldots, U_{i,b+s}] & s = -3, -2, -1 \\ [U_{i,s+1}, \ldots, U_{i,b}, U_{i,1}, \ldots, U_{i,s}] & s = 0, 1, 2, 3. \end{cases} \tag{11}$$

The dimension of vector E_i^s is b, which needs to be compressed to a_i as follows:

$$D_i^s = \left[\sum_{j=1}^{c} T_{i,j}^s, \sum_{j=c+1}^{2c} T_{i,j}^s, \ldots, \sum_{j=(a_i-1)c+1}^{b} T_{i,j}^s\right], \quad c = b/a_i \tag{12}$$

According to (12), b is a common multiple of $a_1, \ldots, a_r$, and $l = 360/b$. For the RAB grid, we set

$$a_i = i \cdot a_1, \quad i = 1, \ldots, r. \tag{13}$$

Therefore, once the RAB grid (a_1) is determined, l can be calculated. Then, for the orientation s, the descriptor vectors of all rings are connected to generate the final descriptor vector D^s as follows:

$$D^s = [D_1^s, \ldots, D_r^s]. \tag{14}$$

In summary, the abovementioned scheme only captures descriptor values once in a regular log-polar grid and can directly generate descriptor vectors with seven orientations. Obviously, descriptor vectors with more orientations can also be generated directly without significantly increasing the computational efficiency. Compared with capturing descriptor values seven times in the RAB grid, this scheme can improve the construction efficiency of the descriptors.

E. Matching Algorithm

After feature detection and description in both the reference and sensed images, the correspondences are selected by the NNDR matching strategy [12] using the Euclidean distance. However, for each feature point in the reference image, there are seven distance values from the corresponding feature point in the sensed image because each feature point in the sensed image has seven descriptor vectors with different orientations. Therefore, we should determine the correct orientation for the feature point in the sensed image.

We use the minimum distance among the seven distances to measure the distance of a match, and there exists an orientation value corresponding to the minimum distance. Note that a match with a smaller distance ratio is more likely to be a correct correspondence. We first extract a set including the top 300 matches with the smallest distance ratio. The corresponding 300 orientation indices can also be obtained. Obviously, the rate of correct match is high for the set. Then, we count the number of

TABLE I
DETAILS OF EXPERIMENTAL DATASETS

NO.	Image source	Band	Polarization	Size (pixels)	GSD (m)	Direction	Date	Location (China)
1	ALOS-PALSAR	L	HH	600×600	30	Descending	09/22/2008	Zhengzhou
	ALOS-PALSAR	L	HH	600×600	30	Ascending	12/22/2008	
2	Gaofen-3	C	HH	820×820	3	Ascending	07/22/2018	Shanghai
	Gaofen-3	C	HH	500×500	5	Ascending	06/18/2018	
3	Gaofen-3	C	VV	750×750	3	Descending	02/24/2018	Shenzhen
	Gaofen-3	C	HH	750×750	3	Ascending	03/03/2018	
4	Sentinel-1	C	VV	800×800	10	Ascending	05/06/2016	Luohe
	Sentinel-1	C	VH	800×800	10	Ascending	05/23/2016	
5	TerraSAR-X	X	HH	500×500	20	Descending	04/18/2009	Tianjin
	ALOS-PALSAR	L	HH	800×800	12.5	Ascending	05/07/2008	
6	Gaofen-3	C	VV	800×800	8	Ascending	04/30/2017	Zhengzhou
	Sentinel-1	C	VV	650×650	10	Ascending	05/23/2016	

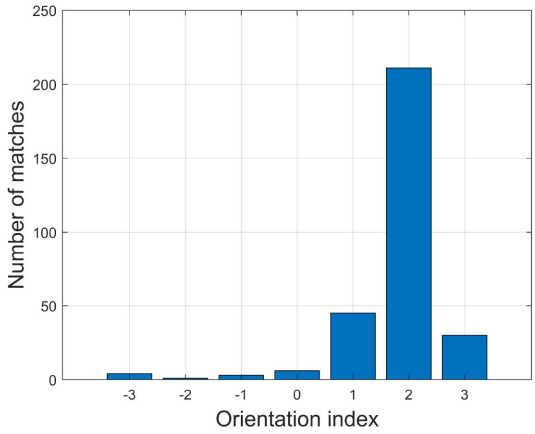

Fig. 6. Number of matches on seven orientation indices for example image pair with rotation angle of 10°.

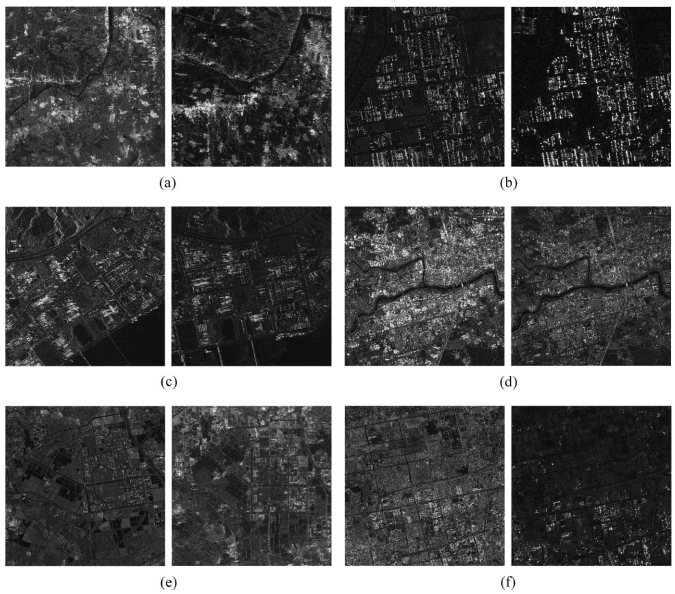

Fig. 7. SAR image pairs. (a)–(f) Correspond to Pairs 1–6.

matches on seven orientation indices. The orientation index with the largest number of matches is effective, and the corresponding orientation is closest to the rotation angle between the two images. Fig. 6 presents the number of matches on seven orientation indices for an example image pair with rotation angle of 10°. The descriptor is captured based on a specific RAB grid with $l = 5°$. As seen, the orientation index is 2, and the orientation is $2l = 10°$, which is equal to the rotation angle. Finally, for each feature point in the sensed image, only the descriptors under the effective orientation are reserved; the others are rejected.

After the abovementioned processing, there is only one descriptor vector for feature points in the sensed image, so stand NNDR matching can be performed to obtain the initial matches. Furthermore, we use the FSC algorithm to remove outliers from the initial matches [32]. The FSC algorithm can robustly extract effective matches from a large number of outliers. However, in FSC, the small distance ratio threshold d_h, which controls the size of the sample set, is sensitive to the image scene. Instead of subjectively setting d_h, we again select the top 300 matches with the smallest distance ratio as the sample set. In addition, the affine transformation model is computed between the reference and sensed images to identify the effective matches by considering a threshold of $2\sqrt{2}$ pixels.

III. EXPERIMENTS AND RESULTS

In this section, we experimentally validate the performance of the proposed SAR image registration method on six SAR image pairs. First, the experimental datasets are introduced. Then, the proposed RRSS descriptor is evaluated. Finally, the registration results are analyzed.

A. Datasets

The experimental data consist of six SAR image pairs, as presented in Table I and Fig. 7. These image pairs are a variety of different bands (*L*, *C*, and *X*), polarizations (HH, VH, and VV), orbit directions (Ascending and Descending), and resolutions from different sensors including ALOS-PALSAR, Gaofen-3,

Sentinel-1, and TerraSAR-X. The two images of each pair are acquired at different times. In terms of geometric differences, Pairs 1, 3, and 5 have obvious rotation differences because they contain two images from different orbit directions. Pairs 2, 5, and 6 have significant scale differences as the ground sampling distances (GSD) of the two images in them are different. Radiometric differences exist between two images of a pair with varying imaging conditions. According to the imaging conditions, these image pairs can be classified into three categories: 1, 2, and 3.

Category 1: Image pairs of this category (Pairs 1 and 2) contain two images from the same sensor in the same polarization.

Category 2: Image pairs of this category (Pairs 3 and 4) contain two images from the same sensor in different polarizations.

Category 3: Image pairs of this category (Pairs 5 and 6) contain two images from different sensors. Furthermore, there is a temporal difference close to 1 year between the images in these two pairs.

The radiometric differences of image pairs in Categories 2 and 3 are relatively large.

B. Descriptor Evaluation

In this section, we evaluate the performance of the proposed RRSS descriptor by comparing it with seven state-of-the-art descriptors (SIFT [12], SURF [35], KAZE [31], SAR-SIFT [17], LSS [24], DOBSS [26], and RLSS [29]). The evaluation criteria, parameter tuning, rotation invariance test, and comparative analysis are presented in the following sections.

1) Evaluation Criteria: In our experiments, the performance of the proposed RRSS descriptor is measured by the recall and precision [11], [42]. The recall and precision values are estimated as follows:

$$\text{recall} = \frac{\text{CM}}{C}, \quad \text{precision} = \frac{\text{CM}}{\text{CM} + \text{FM}} \tag{15}$$

where C is the total number of existing correspondences in the feature point sets. CM and FM are the number of correct matches and false matches in the initial matches, respectively. With the threshold of NNDR spanned between 0.9 and 1 with a step of 0.02, different recall and precision values can be obtained. Then, the precision versus recall curve can be drawn. The higher the recall or precision, the better the robustness of the descriptor to the image scene.

To identify the correct matches, 40–60 evenly distributed points are manually selected as check points to compute the projective transformation model between the images of each pair. The obtained transformation is used to identify the correct matches by considering a threshold value of $\sqrt{2}$ pixels.

2) Parameter Tuning: The proposed RRSS descriptor contains three key parameters, namely, the radius of neighborhood $k\sigma$, the number of radial bins r, and the number of angular bins $A = \{a_1, \ldots, a_r\}$. k should not be too small or too large. The former makes it difficult for the descriptor to describe features discriminatively, while the latter increases the sensitivity of the descriptor to the local geometric distortion. The other two parameters determine the density of the RAB grid. A grid with appropriate density can ensure the distinctiveness of the descriptor. In addition, if the density is excessive, then the descriptor will be overdimensional, resulting in low computational efficiency.

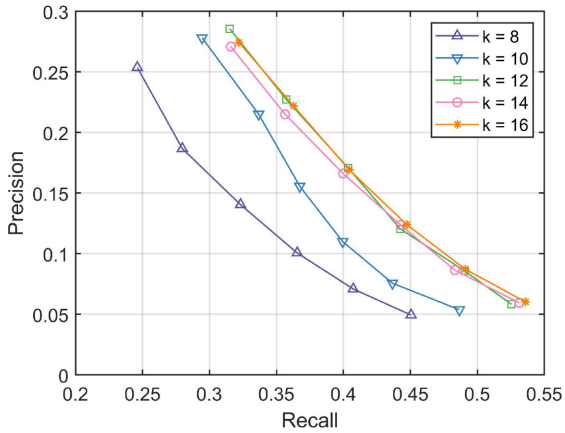

Fig. 8. Average precision versus recall curves of six image pairs fo r different k.

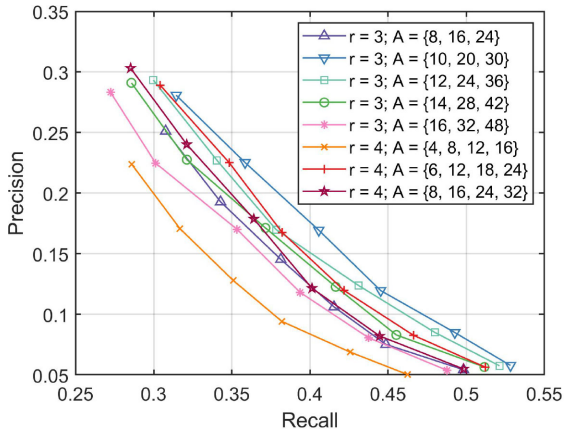

Fig. 9. Average precision versus recall curves of six image pairs for different combinations of r and A.

To evaluate the influence of k on the descriptor, experiments are conducted on six image pairs (see Table I) with different k. In the experiments, k varies from 8 to 16 with an interval of 2; r and A take fixed values, $r = 3$, $A = \{10, 20, 30\}$. Fig. 8 presents the average precision versus recall curves of six image pairs for different k. As seen, the performance of the RRSS descriptor is close to optimal when k reaches 12 and only slightly changes as k continues to increase. Therefore, $k = 12$ is chosen as the optimum value in the following experiments.

To evaluate the influence of r and A, experiments are conducted on six image pairs (see Table I) with different combinations of r and A. In the combinations, two different values (3 and 4) are considered for r, and eight sets $\{8, 16, 24\}$, $\{10, 20, 30\}$, $\{12, 24, 36\}$, $\{14, 28, 42\}$, $\{16, 32, 48\}$, $\{4, 8, 12, 16\}$, $\{6, 12, 18, 24\}$, and $\{8, 16, 24, 32\}$ are considered for A. k is set to a fixed value in the experiments, $k = 12$. Fig. 9 presents the average precision versus recall curves of six image pairs for different combinations of r and A. As seen, the performance of the RRSS descriptor varies with

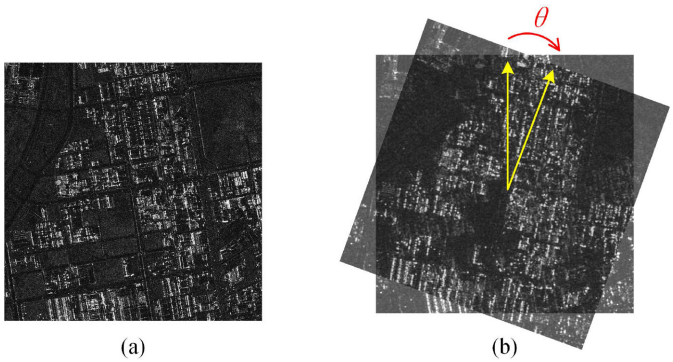

Fig. 10. Example image pair (Pair 2) contains (a) reference image and (b) sensed image.

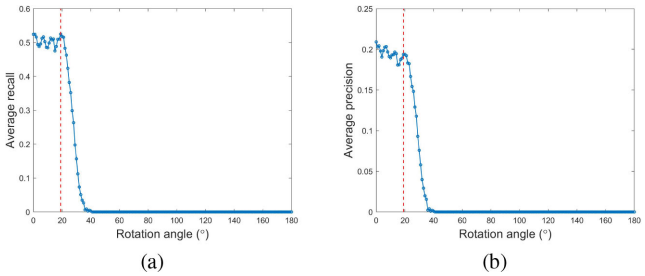

Fig. 11. (a) Average recall and (b) precision of three image pairs with respect to rotation angle when the orientation number is 7.

different combinations. Better results are obtained for $r = 3$ and $A = \{10, 20, 30\}$, which are considered optimum values for the RRSS descriptor in the following experiments. For the selected parameters, the orientation spacing l is $6°$, and the dimension of the RRSS descriptor is 120.

3) Rotation Invariance Test: To test the rotation invariance of the proposed RRSS descriptor, experiments are conducted on Pairs 2, 4, and 6 (see Table I). There are almost no rotation differences in these three pairs. For each of the three pairs, the reference image is rotated clockwise at a certain angle θ, as shown in Fig. 10, and matched with the sensed image. The recall and precision can be obtained by setting the threshold of NNDR to 0.94. The average recall and precision of three image pairs are counted as the rotation angle θ varies from $0°$ to $180°$ with an interval of $1°$.

Fig. 11 shows the average recall and precision of three image pairs with respect to the rotation angle when the orientation number is 7. When the rotation angle is less than $19°$, the average recall and precision remain stable with slight fluctuations. When the rotation angle is increased to $19°$, the average recall and precision drop rapidly, and the matching performance degrades. When the rotation angle reaches $40°$, the average recall and precision are 0, and the matching fails. This occurs because the RRSS descriptor acquires descriptor vectors in seven orientations with a spacing of $6°$ to enhance the rotation invariance, and thus, the maximum rotation difference that the descriptor can resist should be slightly greater than $18°$. This maximum rotation difference can satisfy the matching scenes of the experiment in this article. Note that the orientation number of the descriptor

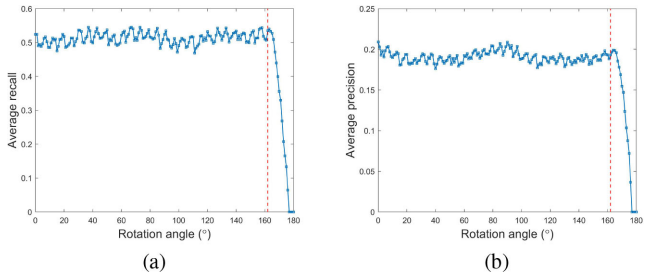

Fig. 12. (a) Average recall and (b) precision of three image pairs with respect to rotation angle when the orientation number is increased to 55.

can be increased to accommodate application scenes with larger rotation differences. This does not significantly reduce the construction efficiency of the descriptor because the acceleration scheme is used in the rotation invariance enhancement method. Fig. 12 shows the average recall and precision of three image pairs with respect to the rotation angle when the orientation number is increased to 55. As seen, the average recall and precision can generally remain stable when the rotation angle is less than $162°$. This confirms the effectiveness of the RRSS descriptor in resisting the rotation differences.

4) Comparative Analysis: To verify the effectiveness of the proposed RRSS descriptor, comparative experiments are conducted on six image pairs (see Table I) with eight descriptors: SIFT, SURF, KAZE, SAR-SIFT, LSS, DOBSS, RLSS, and RRSS. SIFT, SURF, KAZE, and SAR-SIFT are gradient-based descriptors, while DOBSS, RLSS, and RRSS are LSS-based descriptors. The RLSS descriptor uses the same rotation invariance enhancement method as the proposed RRSS descriptor, which is based on the RAB grid.

Fig. 13 presents the precision versus recall curves of eight descriptors for six image pairs. As seen, the RRSS descriptor significantly outperforms the other descriptors in all six image pair cases. The reason for this is that the ratio surface is robust to speckles, and the rank surface can effectively express local shape information. Furthermore, the unreliable process of orientation assignment is avoid. Therefore, the RRSS descriptor can describe features discriminatively.

After the RRSS, better results are achieved by the RLSS and SAR-SIFT. Similar to the RRSS, the RLSS descriptor also constructs the rank surface to enhance its discriminability, and thus, they achieve better performance than other LSS-based descriptors. The SAR-SIFT descriptor calculates the gradient by ratio to reduce the interference of speckles. For this reason, the SAR-SIFT performs better than other gradient-based descriptors.

C. Registration Analysis

In this section, we analyze the registration performance of the proposed method by comparing it with three advanced methods: SIFT [12], KAZE [31], and SAR-SIFT [17]. The following sections present the evaluation criteria and comparative analysis.

1) Evaluation Criteria: In the experiments, the performance of the proposed registration method is quantitatively evaluated by four criteria: CM, precision, root-mean-square error (RMSE),

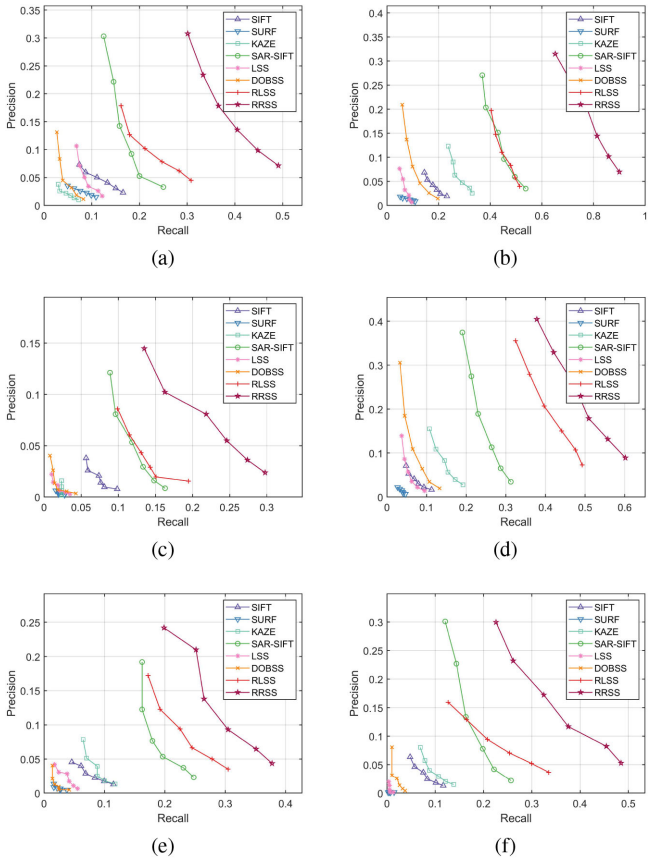

Fig. 13. Precision versus recall curves of eight descriptors for six image pairs. (a)–(f) Correspond to Pairs 1–6.

TABLE II
REGISTRATION PERFORMANCE OF SIFT, KAZE, SAR-SIFT, AND PROPOSED METHOD FOR SIX IMAGE PAIRS

NO.	Criterion	SIFT	KAZE	SAR-SIFT	Proposed
1	CM	41	5	51	133
	Precision	0.621	0.5	0.463	0.636
	RMSE	0.77	0.718	0.905	0.766
2	CM	46	83	86	215
	Precision	0.429	0.474	0.351	0.484
	RMSE	0.855	0.839	0.961	0.845
3	CM	3	6	22	63
	Precision	0.2	0.24	0.247	0.466
	RMSE	0.778	0.892	0.97	0.767
4	CM	41	105	138	321
	Precision	0.585	0.6	0.423	0.603
	RMSE	0.854	0.853	0.963	0.836
5	CM	12	20	43	50
	Precision	0.48	0.487	0.346	0.495
	RMSE	0.76	0.88	0.987	0.810
6	CM	19	51	49	156
	Precision	0.475	0.566	0.347	0.545
	RMSE	0.859	0.898	0.941	0.827

TABLE III
AVERAGE PT OF SIFT, KAZE, SAR-SIFT, AND PROPOSED METHOD FOR SIX IMAGE PAIRS

Criterion	SIFT	KAZE	SAR-SIFT	Proposed
Average PT (s)	4.3	4.7	51.3	49.7

and processing time (PT). CM and precision are calculated based on the final matches, which are obtained after outlier removal using the FSC algorithm. A higher value of CM or precision indicates a better performance of the registration method. RMSE is computed with the correct matches to evaluate the positional accuracy. It is defined as follows:

$$\mathrm{RMSE} = \sqrt{\frac{1}{CM}\sum_{i=1}^{CM}(\Delta x_i^2 + \Delta y_i^2)} \tag{16}$$

where Δx_i and Δy_i are the residual errors of the correct matches in the vertical and horizontal directions, respectively. A smaller RMSE value corresponds to a higher positional accuracy.

PT is a measure that evaluates the computational efficiency. An analysis of PT is carried out on a laptop with an Intel(R) Core(TM) i7-8750H 2.20-GHz CPU, 32 GB RAM, and NVIDIA Quadro P1000 graphics card.

2) Comparative Analysis: To analyze the registration performance, comparative experiments are conducted on six image pairs (see Table I) with four methods: SIFT, KAZE, SAR-SIFT, and the proposed method. SIFT constructs Gaussian scale spaces for feature detection and description. KAZE detects and describes features in nonlinear scale spaces to achieve high repeatability and distinctiveness. SAR-SIFT calculates the gradient by ratio instead of differential to improve the robustness to speckles. For these methods, almost all parameter settings follow the recommendations of their author, except that the contrast threshold is fine-tuned to ensure that they extract approximately equal numbers of feature points. All methods use the same matching method (NNDR and FSC).

Table II compares the registration performance in terms of CM, precision, and RMSE. The proposed method is capable of robustly registering SAR images and generally outperforms SIFT, KAZE, and SAR-SIFT in terms of CM and precision (especially CM). This is mainly because the RRSS descriptor is used in the proposed method. The RRSS descriptor can suppress image speckles, discriminate local features robustly, and avoid the unreliable process of orientation assignment. In terms of RMSE, the performances of SIFT, KAZE, and the proposed method are close and better than that of SAR-SIFT for all six image pairs. Note that the positional accuracy of the matching depends more on the type of feature detector than the type of feature descriptor [27]. Therefore, the reason for the RMSE performance is that SIFT, KAZE, and the proposed method detect feature points with subpixel precision, while SAR-SIFT can only obtain feature points with pixel precision.

Table III presents the average PT of SIFT, KAZE, SAR-SIFT, and proposed method for six image pairs. The average PT result of the proposed method is slightly better than that of SAR-SIFT but obviously inferior to the results of SIFT and KAZE. One of the reasons is that SIFT and KAZE are implemented in C++, while SAR-SIFT and the proposed method are implemented in MATLAB.

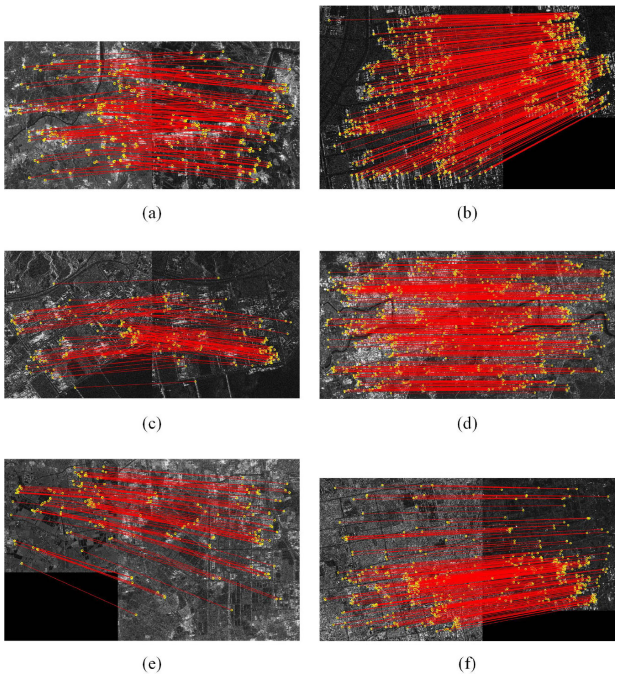

Fig. 14. Matching results of the proposed method for six image pairs. (a)–(f) Correspond to Pairs 1–6.

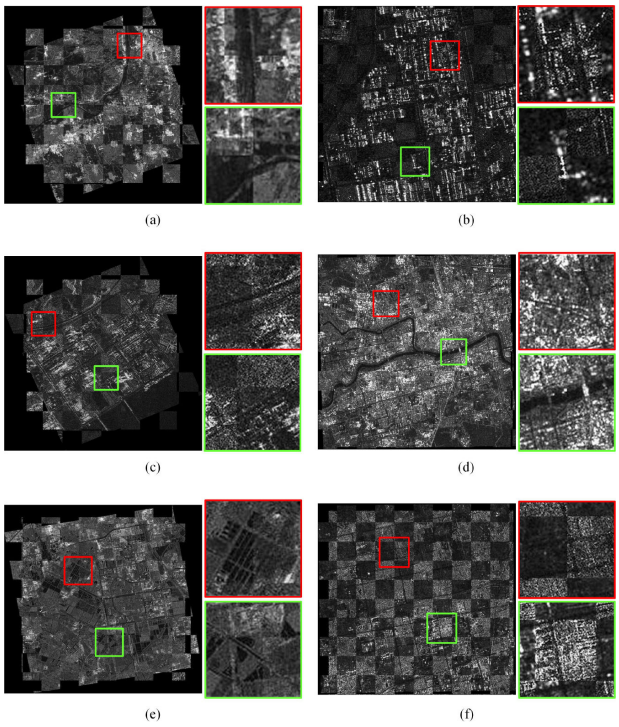

Fig. 15. Registration results of the proposed method for six image pairs. (a)–(f) correspond to Pairs 1–6.

Figs. 14 and 15 show the matching and registration results of the proposed method for six image pairs, respectively. The results show that the proposed method can detect a sufficient number of matches and is suitable for various SAR image registration.

IV. Conclusion

In this article, a novel feature descriptor named RRSS is proposed for reliable SAR image registration. The descriptor calculates the ratio surface to suppress the speckles and extracts the rank surface to enhance the discriminability. Furthermore, to avoid the process of orientation assignment, a rotation invariance enhancement method is designed to efficiently calculate descriptor vectors in multiple orientations. We conduct extensive experiments using six SAR image pairs of various bands, polarizations, and resolutions from different sensors. The results demonstrate the superiority of the proposed descriptor over several state-of-the-art descriptors. The registration results also confirm the effectiveness and robustness of the proposed descriptor for SAR image registration.

Note that a comparable PT is required for image registration using the proposed descriptor. Therefore, our future work will focus on improving computational efficiency.

Acknowledgment

The authors would like to thank the associate editor and reviewers for their helpful comments and good suggestions.

References

[1] X. Xiong, G. Jin, Q. Xu, H. Zhang, and J. Xu, "Robust line detection of synthetic aperture radar images based on vector radon transformation," *IEEE J. Sel. Top. Appl. Earth Observ. Remote Sens.*, vol. 12, no. 12, pp. 5310–5320, Dec. 2019.

[2] E. Sansosti, P. Berardino, M. Manunta, F. Serafino, and G. Fornaro, "Geometrical SAR image registration," *IEEE Trans. Geosci. Remote Sens.*, vol. 44, no. 10, pp. 2861–2870, Oct. 2006.

[3] B. Zitov and J. Flusser, "Image registration methods: A survey," *Image Vis. Comput.*, vol. 21, no. 11, pp. 977–1000, 2003.

[4] S. Suri and P. Reinartz, "Mutual-information-based registration of TerraSAR-X and ikonos imagery in urban areas," *IEEE Trans. Geosci. Remote Sens.*, vol. 48, no. 2, pp. 939–949, Feb. 2010.

[5] J. C. Yoo and T. H. Han, "Fast normalized cross-correlation," *Circuits Syst. Signal Process.*, vol. 28, no. 2, pp. 144–156, 2009.

[6] F. Wang and B. C. Vemuri, "Non-rigid multi-modal image registration using cross-cumulative residual entropy," *Int. J. Comput. Vis.*, vol. 74, no. 2, pp. 201–215, 2007.

[7] L. Pallotta, G. Giunta, and C. Clemente, "SAR image registration in the presence of rotation and translation: A constrained least squares approach," *IEEE Geosci. Remote Sens. Lett.*, to be published, doi: 10.1109/LGRS.2020.3005198.

[8] L. Pallotta, G. Giunta, and C. Clemente, "Subpixel SAR image registration through parabolic interpolation of the 2-D cross correlation," *IEEE Trans. Geosci. Remote Sens.*, vol. 58, no. 6, pp. 4132–4144, Jun. 2020.

[9] A. Sedaghat, M. Mokhtarzade, and H. Ebadi, "Uniform robust scale-invariant feature matching for optical remote sensing images," *IEEE Trans. Geosci. Remote Sens.*, vol. 49, no. 11, pp. 4516–4527, Nov. 2011.

[10] R. Feng, Q. Du, X. Li, and H. Shen, "Robust registration for remote sensing images by combining and localizing feature- and area-based methods," *ISPRS J. Photogrammetry Remote Sens.*, vol. 151, pp. 15–26, 2019.

[11] Y. Ye, J. Shan, S. Hao, L. Bruzzone, and Y. Qin, "A local phase based invariant feature for remote sensing image matching," *ISPRS J. Photogrammetry Remote Sens.*, vol. 142, pp. 205–221, 2018.

[12] D. G. Lowe, "Distinctive image features from scale-invariant keypoints," *Int. J. Comput. Vis.*, vol. 60, no. 2, pp. 91–110, 2004.

[13] P. Schwind, S. Suri, P. Reinartz, and A. Siebert, "Applicability of the SIFT operator to geometric SAR image registration," *Int. J. Remote Sens.*, vol. 31, no. 8, pp. 1959–1980, 2010.

[14] S. Wang, H. You, and K. Fu, "BFSIFT: A novel method to find feature matches for SAR image registration," *IEEE Geosci. Remote Sens. Lett.*, vol. 9, no. 4, pp. 649–653, Jul. 2011.

[15] F. Wang, H. You, and X. Fu, "Adapted anisotropic Gaussian SIFT matching strategy for SAR registration," *IEEE Geosci. Remote Sens. Lett.*, vol. 12, no. 1, pp. 160–164, Jan. 2015.
[16] J. Fan, Y. Wu, F. Wang, Q. Zhang, G. Liao, and M. Li, "SAR image registration using phase congruency and nonlinear diffusion-based SIFT," *IEEE Geosci. Remote Sens. Lett.*, vol. 12, no. 3, pp. 562–566, Mar. 2015.
[17] F. Dellinger, J. Delon, Y. Gousseau, J. Michel, and F. Tupin, "SAR-SIFT: A SIFT-like algorithm for SAR images," *IEEE Trans. Geosci. Remote Sens.*, vol. 53, no. 1, pp. 453–466, Jan. 2015.
[18] H. Goncalves, L. Corte-Real, and J. A. Goncalves, "Automatic image registration through image segmentation and SIFT," *IEEE Trans. Geosci. Remote Sens.*, vol. 49, no. 7, pp. 2589–2600, Jul. 2011.
[19] B. Wang, J. Zhang, L. Lu, G. Huang, and Z. Zhao, "A uniform SIFT-like algorithm for SAR image registration," *IEEE Geosci. Remote Sens. Lett.*, vol. 12, no. 7, pp. 1426–1430, Jul. 2015.
[20] S. Paul and U. C. Pati, "A block-based multifeature extraction scheme for SAR image registration," *IEEE Geosci. Remote Sens. Lett.*, vol. 15, no. 9, pp. 1387–1391, Sep. 2018.
[21] S. Paul and U. C. Pati, "SAR image registration using an improved SAR-SIFT algorithm and Delaunay-triangulation-based local matching," *IEEE J. Sel. Top. Appl. Earth Observ. Remote Sens.*, vol. 12, no. 8, pp. 2958–2966, Aug. 2019.
[22] Y. Xiang, F. Wang, L. Wan, and H. You, "An advanced rotation invariant descriptor for SAR image registration," *Remote Sens.*, vol. 9, no. 7, pp. 686–697, 2017.
[23] L. Zeng, D. Zhou, J. Liang, and K. Zhang, "Polar scale-invariant feature transform for synthetic aperture radar image registration," *IEEE Geosci. Remote Sens. Lett.*, vol. 14, no. 7, pp. 1–5, Jul. 2017.
[24] E. Shechtman and M. Irani, "Matching local self-similarities across images and videos," in *Proc. IEEE Comput. Vis. Pattern Recognit*. Minneapolis, MN, USA, Jun. 2007, vol. 2, pp. 1–8.
[25] Y. Ye and J. Shan, "A local descriptor based registration method for multispectral remote sensing images with non-linear intensity differences," *ISPRS J. Photogrammetry Remote Sens.*, vol. 90, pp. 83–95, 2014.
[26] A. Sedaghat and H. Ebadi, "Distinctive order based self-similarity descriptor for multi-sensor remote sensing image matching," *ISPRS J. Photogrammetry Remote Sens.*, vol. 108, pp. 62–71, 2015.
[27] A. Sedaghat and N. Mohammadi, "Illumination-robust remote sensing image matching based on oriented self-similarity," *ISPRS J. Photogrammetry Remote Sens.*, vol. 153, pp. 21–35, 2019.
[28] Y. Ye, L. Shen, M. Hao, J. Wang, and Z. Xu, "Robust optical-to-SAR image matching based on shape properties," *IEEE Geosci. Remote Sens. Lett.*, vol. 14, no. 4, pp. 564–568, Apr. 2017.
[29] X. Xiong, Q. Xu, G. Jin, H. Zhang, and X. Gao, "Rank-based local self-similarity descriptor for optical-to-SAR image matching," *IEEE Geosci. Remote Sens. Lett.*, vol. 17, no. 10, pp. 1742–1746, Oct. 2020.
[30] P. Alcantarilla, J. Nuevo and A. Bartoli, "Fast explicit diffusion for accelerated features in nonlinear scale spaces," in *Proc. Brit. Mach. Vis. Conf.*, 2013, pp. 1–12.
[31] P. F. Alcantarilla, A. Bartoli, and A. J. Davison, "Kaze features," in *Proc. Eur. Conf. Comput. Vis*., 2012, pp. 214–227.
[32] Y. Wu, W. Ma, M. Gong, L. Su, and L. Jiao, "A novel point-matching algorithm based on fast sample consensus for image registration," *IEEE Geosci. Remote Sens. Lett.*, vol. 12, no. 1, pp. 43–47, Jan. 2015.
[33] E. Rosten, R. Porter, and T. Drummond, "Faster and better: A machine learning approach to corner detection," *IEEE Trans. Pattern Anal. Mach. Intell.*, vol. 32, no. 1, pp. 105–119, Jan. 2010.
[34] C. G. Harris and M. Stephens, "A combined corner and edge detector," in *Proc. Alvey Vis. Conf*., 1988, pp. 147–151.
[35] H. Bay, A. Ess, T. Tuytelaars, and L. Van Gool, "Speeded-up robust features (SURF)," *Comput. Vis. Image Understanding*, vol. 110, no. 3, pp. 346–359, 2008.
[36] J. Fan, Y. Wu, M. Li, W. Liang, and Y. Cao, "SAR and optical image registration using nonlinear diffusion and phase congruency structural descriptor," *IEEE Trans. Geosci. Remote Sens.*, vol. 56, no. 9, pp. 5368–5379, Sep. 2018.
[37] C. Spearman, "The proof and measurement of association between two things," *Int. J. Epidemiol.*, vol. 39, no. 5, pp. 1137–1150, 2010.
[38] K. Mikolajczyk and C. Schmid, "A performance evaluation of local descriptors," *IEEE Trans. Pattern Anal. Mach. Intell.*, vol. 27, no. 10, pp. 1615–1630, Oct. 2005.
[39] E. Tola, V. Lepetit, and P. Fua, "DAISY: An efficient dense descriptor applied to wide-baseline stereo," *IEEE Trans. Pattern Anal. Mach. Intell.*, vol. 32, no. 5, pp. 815–830, May 2010.
[40] A. Sedaghat and H. Ebadi, "Remote sensing image matching based on adaptive binning SIFT descriptor," *IEEE Trans. Geosci. Remote Sens.*, vol. 53, no. 10, pp. 5283–5293, Oct. 2015.
[41] B. Fan, C. Huo, C. Pan, and Q. Kong, "Registration of optical and SAR satellite images by exploring the spatial relationship of the improved SIFT," *IEEE Geosci. Remote Sens. Lett.*, vol. 10, no. 4, pp. 657–661, Jul. 2013.
[42] M. Gesto-Diaz, F. Tombari, D. Gonzalez-Aguilera, L. Lopez-Fernandez, and P. Rodriguez-Gonzalvez, "Feature matching evaluation for multimodal correspondence," *ISPRS J. Photogrammetry Remote Sens.*, vol. 129, pp. 179–188, 2017.

Xin Xiong received the B.S. and M.S. degrees in photogrammetry and remote sensing from the Institute of Geospatial Information, Information Engineering University, Zhengzhou, China, in 2014 and 2017, respectively. He is currently working toward the Ph.D. degree with Information Engineering University, Zhengzhou, China.

His research interests include image feature extraction and matching.

Guowang Jin received the B.S., M.S., and Ph.D. degrees in photogrammetry and remote sensing from the Institute of Geospatial Information, Information Engineering University, Zhengzhou, China, in 2000, 2003 and 2007, respectively.

He is currently a Professor and a Doctoral Supervisor with Information Engineering University. His research interests include radargrammetry and synthetic aperture radar (SAR) interferometry.

Qing Xu received the B.S., M.S., and Ph.D. degrees in photogrammetry and remote sensing from the Institute of Geospatial Information, Information Engineering University, Zhengzhou, China, in 1985, 1990 and 1995, respectively.

He is currently a Professor and a Doctoral Supervisor with Information Engineering University, Zhengzhou, China. His research interests include photogrammetry and deep space remote sensing mapping.

Dr. Xu has been a member of the Professional Committee of the Photogrammetry and Remote sensing of the Chinese Society for Geodesy, Photogrammetry and Cartography (CSGPC) since 2000. Since 2004, he has been a member of the Professional Committee of the Deep Space Exploration of the Chinese Society of Astronautics (CSA). Since 2006, he has been a member of the Expert Committee of the Scientific Application of the Exploring Project around the Moon.

Hongmin Zhang received the B.S., M.S., and Ph.D. degrees in photogrammetry and remote sensing from the Institute of Geospatial Information, Information Engineering University, Zhengzhou, China, in 2007, 2010 and 2013, respectively.

She is currently an Associate Professor with Information Engineering University. Her research interests include radar signal processing and radargrammetry.